Nature Communications

https://doi.org/10.1038/s41467-026-70630-w

Article in Press

Water as a gas separation membrane

Received: 8 September 2025

Accepted: 27 February 2026

Cite this article as: Lopez, K.P., Saffer-Meng, M., Allouzi, M. *et al.* Water as a gas separation membrane. *Nat Commun* (2026). https://doi.org/10.1038/s41467-026-70630-w

Kian P. Lopez, Max Saffer-Meng, Mohammad Allouzi, Yukai Tomsovic, Joshua N. Sherrit, Sasha R. Neefe, Patrick O. Saboe, Mou Paul, Abhishek Roy & Anthony P. Straub

Water as a gas separation membrane

Nature Communications

Kian P. Lopez[1], Max Saffer-Meng[1], Mohammad Allouzi[2,3], Yukai Tomsovic[2,4], Joshua N. Sherrit[1], Sasha R. Neefe[1], Patrick O. Saboe[5], Mou Paul[5], Abhishek Roy[5], and Anthony P. Straub[2,3,4*]

[1]Department of Chemical & Biological Engineering, University of Colorado Boulder, Boulder, CO 80303, USA
[2]Department of Mechanical and Process Engineering, ETH Zürich, Zürich 8092, Switzerland
[3]Department of Civil, Environmental & Architectural Engineering, University of Colorado Boulder, Boulder, CO 80303, USA
[4]Materials Science & Engineering Program, University of Colorado Boulder, Boulder, CO 80303, USA
[5]National Laboratory of the Rockies, Golden, CO, 80401, USA

[*]Corresponding author:
Anthony Straub, Email: astraub@ethz.ch

Abstract

Efficient gas separation membranes are essential for carbon capture, biogas upgrading, and hydrogen purification. Inspired by how plants absorb CO_2 through water, we present a membrane platform that uses liquid water as the selective layer. Hydrophilic sub-100-nm pores stabilize water through strong capillary forces, enabling operation at feed pressures above 72 bar under dry and humid conditions. Selectivity is governed by gas solubility in water, while permeance is tuned by adjusting the water layer thickness. Reducing this thickness below 200 nm yields CO_2 permeances up to 11,600 gas permeation units with CO_2:N_2, CO_2:CH_4, and CO_2:H_2 selectivities of 40, 26, and 31, surpassing the performance of state-of-the-art membranes. Operation is sustained for over a week without water loss, and performance scales using commercially available porous polymer supports under mixed-gas crossflow conditions. Water's dissolution-based transport avoids saturation and reaction-rate limits, enabling a robust, high-performance, and environmentally benign gas separation platform.

Gas separations are crucial to industrial and environmental processes such as carbon capture, biomethane purification, and syngas upgrading, where efficient separation of CO_2 from gases like N_2, CH_4, and H_2 is necessary[1–3]. Membrane-based gas separations have the potential to be up to ten-times more energy efficient than conventional technologies, such as amine scrubbing and cryogenic separation, while also offering simpler operation and modular design[4–8]. However, current membranes are fundamentally limited by the trade-off between permeance and selectivity, where most membranes exhibit moderate selectivity but their throughput is constrained by low CO_2 permeance[9,10]. Furthermore, many widely considered membrane materials are susceptible to plasticization or physical degradation when exposed to high-pressure and humid conditions, limiting their use in real-world applications[11–16].

Supported liquid membranes, which consist of a porous support impregnated with a gas-selective liquid phase, have shown promise in addressing some limitations of current materials. The liquid used, commonly an ionic liquid or amine, can be tailored to selectively interact with CO_2 via favorable physical and chemical interactions, allowing for exceptionally high CO_2 selectivities. However, the gas permeance of supported liquid membranes is often limited by low gas diffusivity, difficulty in making thin liquid layers[15,17], and slow reaction kinetics in certain liquids that rely on chemical reactions with CO_2[18]. In addition, many supported liquid membranes exhibit performance losses as CO_2 partial pressure increases due to saturation of chemical sorption sites, and experience liquid displacement or blowout at relatively low pressures (less than 5 bar)[19,20]. Thus, there is a need to explore material systems that are more permeable, selective, and robust under pressure.

In nature, water plays a central role in gas separations: the two largest carbon sinks on Earth, oceans and plants, both rely on liquid water as a medium to absorb CO_2[21,22]. Plants, in particular, have evolved to uptake CO_2 by dissolving it in water-filled nanochannels lining the walls of leaf mesophyll cells (Figure 1a)[23–25]. The gas–liquid interfaces in these channels both serve as a platform to absorb CO_2 for photosynthesis and sustain the large negative pressures (up to 150 bar) needed to drive water up from the roots using strong capillary forces[26,27]. Nature therefore leverages two unique properties of water in its CO_2 uptake mechanism: (i) water has high CO_2 solubility through physical dissolution and (ii) water has a high surface tension that allows it to remain stable in nanoscale capillaries under high pressure differences[25]. Despite these promising properties of water for gas separations, relatively few studies have explored water in an engineered

gas separation membrane. Prior work has incorporated carbonic anhydrase, ionic liquids, or other reactive chemicals into an aqueous layer to enable facilitated transport[3,28,29], but membranes that mimic the high-pressure tolerance of capillary-stabilized water observed in leaves to improve CO_2 separations remain unexplored.

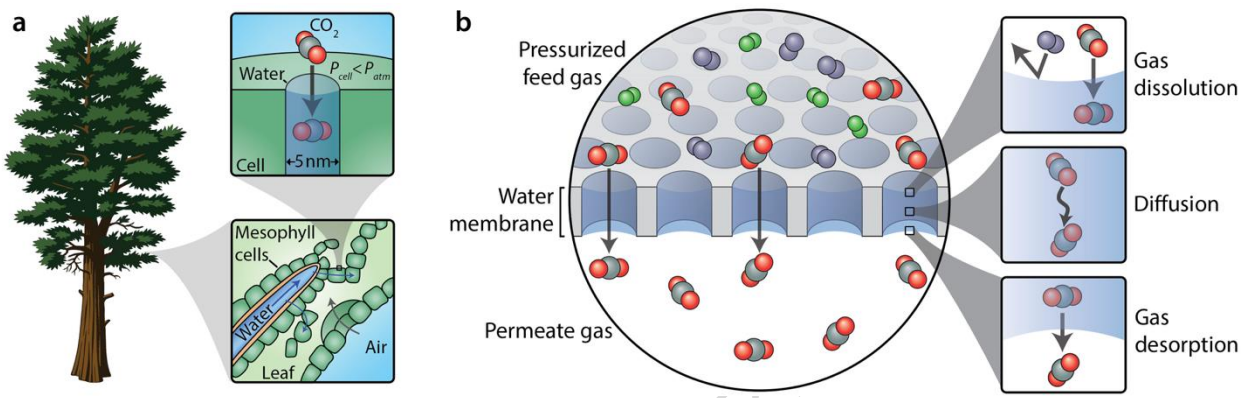

Fig. 1. | Water membranes for gas separations. a, Schematic diagram of CO_2 uptake in trees where CO_2 dissolves into water-filled nanochannels in the wall of leaf mesophyll cells. Capillary forces and water evaporation generate lower pressures inside the cell water channels, P_{cell}, than in the atmosphere, P_{atm}. These negative pressures, up to 150 bar, drive water uptake through the roots and water flow up the xylem water channels. **b**, Schematic diagram of water-based membranes for gas separations, where a layer of water is stabilized within hydrophilic pores. To transport through the membrane, feed gases must dissolve in the water, diffuse through the layer in the aqueous phase, and desorb on the permeate side of the membrane. CO_2 is preferentially transported because of its higher solubility in water compared to other gases.

Inspired by the mechanisms of carbon capture in nature, we explore membranes that use water as a selective layer for gas separations. These membranes employ hydrophilic nanopores to stabilize a thin, pressure-stable water layer (Figure 1b). To transport through the membrane, gases must dissolve in the water, diffuse through the liquid layer, and desorb on the permeate side of the membrane. We use experiments and theory to probe gas transport behavior in these membranes, finding that selectivity is primarily governed by gas solubility in water which results in high CO_2 permeance relative to other gases. By decreasing the thickness of the water layer, we show that gas permeance can be increased without sacrificing selectivity, allowing the membrane to exceed the perm-selectivity limits of state-of-the-art materials in key separations. Furthermore, we

investigate the ability of nanoscale pores to stabilize the water layer under high applied pressure and enable days-long operation of the process without changes in performance. We also explore scale up with commercial, large-scale porous polymer membranes and demonstrate consistent performance under mixed-gas conditions relevant to practical applications. Overall, this work provides a proof-of-concept demonstration for high performance gas separation membranes leveraging liquid water.

Results

Principles of liquid water membranes

Gas transport through liquid water membranes proceeds through a solution-diffusion mechanism, in which gases first dissolve at the feed-side gas–liquid interface, diffuse through the water layer, and then desorb into the gas phase on the permeate side[30]. The dissolved gas concentration at the gas–liquid interface is defined by Henry's law:

$$C_g = K_H \cdot P_g \qquad (1)$$

where C_g is the dissolved gas concentration, K_H is the Henry's constant, and P_g is the gas partial pressure. A difference in the gas partial pressure across the membrane, ΔP_g, leads to a concentration gradient of dissolved gas across the membrane that drives gas flux, J, as described by Fick's first law of diffusion:

$$J = -D\frac{dC_g}{dx} \qquad (2)$$

where D is the diffusion coefficient of the respective gas in water and $\frac{dC_g}{dx}$ is the concentration gradient of dissolved gas over length x. Combining equations (1) and (2) yields a flux expression in terms of known parameters:

$$J = \frac{DK_H}{l}\Delta P_g \qquad (3)$$

where l is the effective water layer thickness. Together, these relations demonstrate that transport is dictated by gas solubility, diffusivity in water, partial pressure gradients, and membrane thickness.

The solution-diffusion model reveals important features of water membrane behavior and design. Since gas diffusivities in liquid water are relatively similar across species, selectivity arises mainly from differences in solubility; these solubility differences are captured by the gas's Henry's

constant which describes the equilibrium partitioning of gas molecules into the water layer. Notably, CO_2 exhibits approximately 40 times higher solubility in water than other gases such as nitrogen, hydrogen, and methane, leading to high selectivity for CO_2. Moreover, since selectivity primarily depends on the Henry's constant, decreasing the thickness of the water layer can increase gas flux without sacrificing selectivity.

To operate effectively, the liquid water layer must remain stably confined within the membrane pores under an applied transmembrane pressure. The maximum pressure the membrane can withstand before gas displaces the water layer, P_{max}, is governed by capillary forces and described by the Young–Laplace equation:

$$P_{max} = \frac{2\gamma cos\theta}{r} \quad (4)$$

where γ is the surface tension of the liquid-gas interface, θ is the intrinsic water contact angle on the membrane surface which serves as an approximation for the receding contact angle, and r is the pore diameter.

In addition to pressure-driven displacement, the stability of water within the pores is also influenced by ambient humidity. At low relative humidities, the confined water phase will evaporate if liquid–vapor equilibrium is not sustained. Capillary forces of water in the nanopore inhibit evaporation by decreasing the equilibrium partial vapor pressure of water, as described by the Kelvin equation:

$$P_v = P_{v,0} \exp\left(-\frac{2\gamma V_w}{r_c RT}\right) \quad (5)$$

where P_v is the vapor pressure at the gas-water interface, $P_{v,0}$ is the equilibrium vapor pressure as a function of temperature, V_w is the water molar volume in the pore, R is the universal gas constant, r_c is the radius of curvature of the liquid-vapor interface, and T is absolute temperature. As ambient humidity decreases, the radius of curvature at the interface must also decrease for vapor–liquid equilibrium to be maintained. The minimum radius of curvature possible in a capillary is a function of the pore radius, r, and the intrinsic water contact angle, θ:

$$r_{c,min} = \frac{r}{cos\theta} \quad (6)$$

If the ambient water vapor pressure drops below the equilibrium pressure corresponding to this minimum curvature, capillary drying occurs, and the water is removed from the pore. Thus, maintaining stable operation of liquid water membranes requires both pressure resistance and

stability under low relative humidity, both of which depend on small, hydrophilic pores to retain the water layer within the membrane.

Experimental gas transport behavior and membrane robustness

To experimentally demonstrate water membranes and validate theory, we tested gas transport performance of water-filled porous membranes using a pressurized gas feed (Figure 2a). Our initial testing used custom-fabricated anodic aluminum oxide membranes with controlled pore diameters (40, 80, 120, 160, and 200 nm) that were impregnated with water simply by pipetting a small droplet on the surface. The thickness of the water layer was varied from 100 μm to 190 nm either by using membranes of different thicknesses (Figure 2a, top inset) or by selectively functionalizing the surface to have a hydrophilic layer of controlled thickness (Figure 2a, bottom inset; Supplementary Note 1; Supplementary Figures 1–3; and Supplementary Table 1). The aluminum oxide membranes provided an ideal platform to explore the fundamental behavior and performance limits of water membranes because (i) they have uniform isopores of known pore size and porosity (Figure 2b,c and Supplementary Figure 4), (ii) they experience minimal deformation under pressure, allowing for reliable measurements, and (iii) they can be functionalized to trap water on the top surface using available surface science techniques (Figure 2d). Although aluminum oxide membranes were advantageous for proof-of-concept testing and model validation, lower cost and more readily scalable materials will likely be used in practice, as we demonstrate later. Characterization of the fabricated membranes is detailed in Supplementary Note 2 and Supplementary Figures 4–10.

Experimental evaluation of the liquid water membranes confirmed their ability to resist water displacement under high applied gas pressures. Young–Laplace theory (equation (4)) predicts that displacement pressure scales inversely with pore diameter, and experimentally measured displacement pressures of membranes with different pore diameters from 40 to 200 nm demonstrated quantitative agreement with values modeled using Young–Laplace (Figure 2e). The highest measured water displacement pressure was 72 bar in the membrane with 40-nm diameter pores. This pressure exceeds the requirements for most applications, including natural gas sweetening and syngas upgrading, where the feed gas pressure can be 20–70 bar[31,32]. The maximum measured displacement pressure is also at least three times higher than values for supported ionic liquid membranes in the literature, which range from 0.1–20 bar[33,20]. We note that

it is possible to achieve even higher displacement pressures using membranes with sub-40-nm pore diameters, but safety limitations in our current experimental setup prevented testing beyond 72 bar.

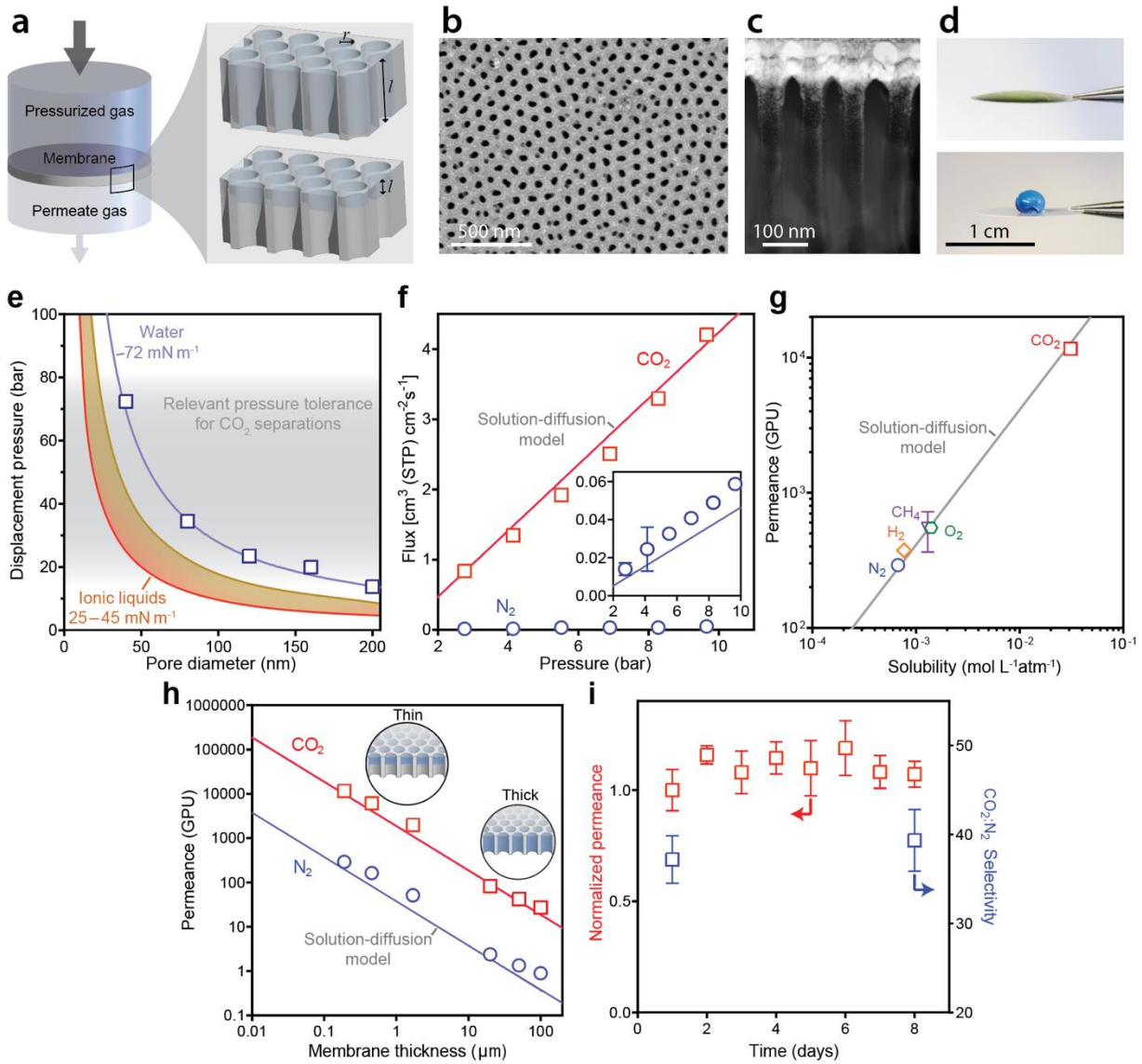

Fig. 2 | Gas separation performance and robustness of the water membrane. a, Schematic of testing setup for gas transport measurements. Inset shows membranes where water fills the entire pore thickness (top) and membranes selectively coated with a hydrophilic water-trapping layer in the upper pore (bottom). In both cases, the pore radius, *r*, and water layer thickness, *l*, could be controlled. **b**, Scanning electron micrograph of the top surface of the anodic alumina membrane with a 40-nm pore diameter. **c,** Scanning transmission electron microscopy high-angle annular dark-field image showing a cross section of the upper pore. **d**, Contact angle of water on the

hydrophilic top surface of the membrane (top) and on the hydrophobic bottom surface of the membrane (bottom). **e**, Measured displacement pressure of the water layer as a function of pore diameter for fabricated membranes (symbols). Theoretical displacement pressures obtained from the Young–Laplace equation using the surface tension of water (72 mN/m) and ionic liquids (25 and 45 mN/m) are also shown[34]. **f**, Measured gas flux as a function of the feed gas pressure for fabricated membranes with 40-nm pore diameters and estimated water layer thicknesses of 287 nm. Lines show gas flux predicted using the solution-diffusion model. Gas flux was normalized to the membrane porosity of 12% so that reported values are representative of the water-filled active pore area. **g**, Measured gas permeance as a function of aqueous solubility for different gases using a membrane pore diameter of 40 nm and an estimated water layer thickness of 190 nm (symbols), and simulated permeance using the solution-diffusion model with a diffusion coefficient of 2.00×10^{-5} $cm^2 \cdot s^{-1}$ (line). **h**, Permeance as a function of the water layer thickness for measurements (symbols) and simulations (lines). **i**, Long-term stability of liquid water membranes over 8 days of operation. Gas permeance was normalized to the initial value. Relative humidity in the feed was limited to less than 1% by continuously venting feed gas. Error bars denote the mean ±1 s.d. for measurements from at least three distinct membrane samples.

Gas flux measurements through the liquid water membranes agree with predictions based on gas dissolution and diffusion theory. The measured gas flux increased linearly with feed gas pressure for CO_2 and N_2 pure gases (Figure 2f). The CO_2 flux was approximately 40-times greater than the N_2 flux, consistent with the difference in aqueous solubility between the two gases. Gas fluxes modeled using solution-diffusion theory with Henry's law for gas solubility and Fick's first law for diffusion (equations (1–3)) showed strong agreement with experimental values using zero fitting parameters.

Permeation experiments with different gases demonstrated that selectivity in the water membrane is primarily governed by the aqueous solubility of each gas (Figure 2g). Experimentally measured gas permeances increased with aqueous gas solubility for N_2, H_2, CH_4, O_2, and CO_2 (Supplementary Table 2). Since most gases have similar diffusion coefficients in water, differences in experimental gas permeances were well-described by the Henry's law constant (Supplementary Table 3 and Supplementary Figure 11). CO_2 exhibited a 24–40 times higher permeance (average of 11,600 gas permeation units, GPU; 1 GPU = 10^{-6} cm^3 [STP] cm^{-2} s^{-1} $cmHg^{-1}$) than other gases

due to its uniquely high solubility arising from strong chemical interactions with water and polarizability.

Decreasing the water layer thickness led to a proportional increase in gas permeance without altering selectivity (Figure 2h). To probe the impact of water layer thickness on transport rates, we fabricated membranes with water layer thicknesses spanning three orders-of-magnitude: 20, 50, and 100 μm thick alumina membranes were tested with water filling their entire thicknesses (Supplementary Figure 12) in addition to membranes with 190 nm, 457 nm, and 1.7 μm thick water layers fabricated using controlled surface modification (Supplementary Notes 1 and 2). Since transport resistances in the membrane are dominated by aqueous-phase diffusion in the liquid water layer, the observed CO_2 permeance of the water layer was inversely proportional to the membrane thickness, increasing from 46 to 11,600 GPU as the thickness decreased from 50 μm to 190 nm. In contrast, prior supported liquid membranes typically employ much thicker active layers on the order of tens of microns, constraining their achievable CO_2 permeances to below 1000 GPU[17,35]. The selectivity between CO_2 and N_2, which is primarily dependent on gas solubility, maintained between 31 and 40 for all membranes regardless of their thickness, showing that permeance can be increased by nearly three orders-of-magnitude by decreasing thickness without compromising selectivity.

Long-term testing showed that the water membranes remained stable over at least eight days of continuous operation with a dry gas feed (Figure 2i). Continuous gas permeation tests were conducted using feed gases with a relative humidity below 1% and an applied pressure of 6.89 bar (Supplementary Figures 13 and 14). The permeate side of the membrane was exposed to water vapor from a condensed water droplet. During the eight-day test, CO_2 permeance showed low variation, and CO_2:N_2 selectivity remained consistent between the first and eighth day of testing. This stability with dry feed conditions can be explained by the vapor pressure depression of water in nanoscale capillaries described by equation (5), with corresponding values given in Supplementary Table 4. By reducing the equilibrium vapor pressure of water in the pores, nanoscale confinement of water both increases the humidity threshold required for evaporation to occur and decreases the driving force when evaporation does take place. Under the tested conditions, these factors slow water loss from the dry feed side and promote net condensation from the permeate side, allowing the water layer to be sustained with only minimal moisture present.

The humidity needed to maintain the water layer is governed by the pore-size-dependent equilibrium vapor pressure described by the Kelvin equation (Supplementary Figure 15).

Permeance and selectivity performance in gas separations

Conventional gas separation membranes are constrained by a trade-off where increases in gas throughput come at the expense of selectivity. In water-based membranes, a key advantage is the ability to reduce the thickness of the water layer without introducing defects, which are a major limitation in polymeric and supported liquid membranes. Since selectivity in the solution-diffusion framework depends only on differences in solubility and diffusivity between species (equation (3)), decreasing the water layer thickness enhances the gas permeance without affecting selectivity, allowing for operation with both high throughput and suitable discrimination between gases.

Gas separation performance for CO_2:N_2 separations, which are critical in carbon capture, demonstrates the ability of liquid water membranes to increase permeance without sacrificing selectivity (Figure 3a). Perm-selectivity trade-offs have historically limited membrane performance for CO_2:N_2 separations, where conventional membranes exhibit an inverse relationship between permeance and selectivity, captured by the Robeson upper bound[36–38]. In contrast, the liquid water membranes show increasing CO_2 permeance with decreasing water layer thickness, reaching values as high as 11,600 GPU with a water layer thickness of 190 nm while maintaining a consistent CO_2:N_2 selectivity of 40:1. This performance exceeds the Robeson upper bound and highlights the potential of liquid water membranes to outperform state-of-the-art materials reported in the literature (Supplementary Table 5). We note that any membrane governed by solution-diffusion should, in theory, be able to similarly increase permeance without sacrificing selectivity since selectivity arises from either solubility or diffusivity differences (equation (3)); in practice, however, fabricating conventional polymer and ionic liquid membranes that are thin and defect-free has been challenging, leading to the trade-off observed in Figure 3a[10].

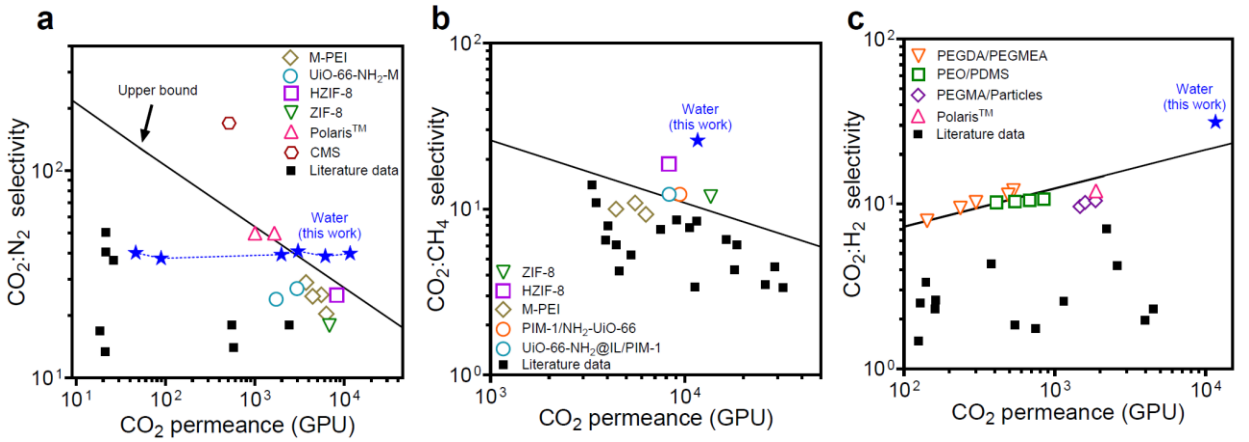

Fig. 3 | Water membranes exceed current permeance and selectivity limits. a, Permeance-selectivity trade-off for CO_2:N_2 with the water membranes studied in this work (blue stars) compared to common values found in the literature (black squares) and the following high performance membranes: Polaris[39], UiO-66-NH_2-M[40], ZIF-8[41], HZIF-8[5], CMS[42], and M-PEI[38]. The Robeson upper bound[9] assuming a thickness of 1 μm is also shown. **b**, Permeance-selectivity trade-off for CO_2:CH_4 compared to literature values and high performance membranes: HZIF-8[5], PIM-1/NH_2-UiO-66[43], ZIF-8[41], UiO-66-NH_2@IL/PIM-1[44], and M-PEI[38]. **c**, Permeance-selectivity performance for CO_2:H_2 compared to the permeance-selectivity upper bound[45] and high performance membranes: PEO/PDMS[46], PEGMA/Particles[47], Polaris[48], and PEGDA/PEGMA[49]. Gas flux is normalized to the active pore area of the membrane based on a porosity of 12%.

In addition to CO_2:N_2 separation, other gas separations such as CO_2:CH_4 and CO_2:H_2 are critical for applications including natural gas upgrading and syngas conditioning[50–52]. Such separations benefit from membranes that maintain suitable selectivity while also achieving high CO_2 permeance. Our membranes demonstrate selectivities of 26 for CO_2:CH_4 and 31 for CO_2:H_2, values that are competitive with state-of-the-art materials. More importantly, these selectivities are sustained at CO_2 permeances exceeding 11,000 GPU, surpassing the performance of conventional membranes that typically operate in the range of 100–5,000 GPU (Figure 3b and 3c). In addition, hydrogen sulfide (H_2S) and ammonia (NH_3), common contaminants in natural gas, biogas, and syngas, are predicted to permeate even faster than CO_2 through liquid water membranes, with theoretical selectivities of up to 3.4 and 1,800 for H_2S:CO_2 and NH_3:CO_2, respectively (Supplementary Figure 16). Our results demonstrate that the high solubility-based selectivity and

low resistance to transport provided by the sub-micron thick water layer enables strong CO_2 separation performance across multiple gas pairs.

Gas sorption capacity and kinetics

In addition to showing high CO_2 permeance, our experiments observed that the permeability of CO_2 in water membranes is maintained even at high CO_2 partial pressures up to 27 bar (Figure 4a). This behavior contrasts with that of ionic liquids and some polymeric membranes, in which CO_2 permeability decreases at elevated partial pressures. The loss of CO_2 permeability in current materials limits CO_2 throughput and causes a loss of selectivity. Mechanistically, ionic liquids experience a loss in CO_2 permeability at high partial pressures because CO_2 sorption decreases as chemical sorption sites become saturated. Sorption of CO_2 in water relies on physical dissolution of gas molecules in water, rather than the formation of carbamate or other chemically bound species and is weakly dependent on CO_2 partial pressure for all practical gas separation scenarios. As a result, CO_2 permeability in liquid water membranes is maintained even at elevated CO_2 partial pressures and, at CO_2 partial pressures above 1 bar, water surpasses the CO_2 permeability of many high-performing ionic liquids. This stability under high CO_2 loadings is particularly advantageous for treating flue gas or natural gas streams, which contain high concentrations of CO_2[53,54].

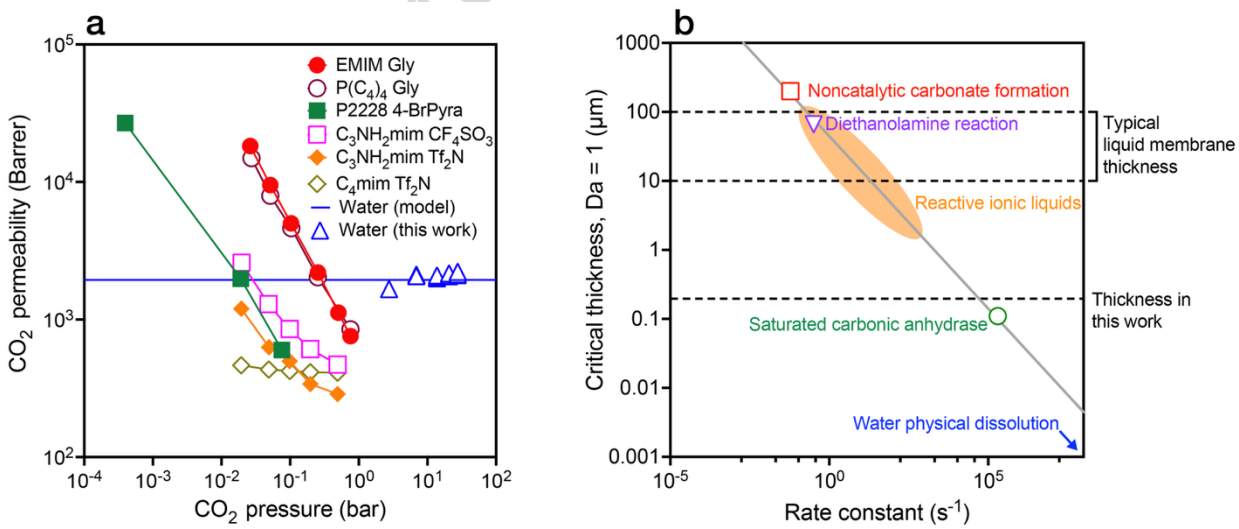

Fig. 4 | Sorption capacity and dissolution kinetics of CO_2 in water. a, CO_2 permeability (Barrer) as a function of CO_2 partial pressure in supported ionic liquid and water membranes. At high CO_2 partial pressure, ionic liquids with high CO_2 solubility can become saturated resulting in lower

CO_2 permeability. Water maintains constant CO_2 permeability at high pressure because CO_2 transport is driven by physical dissolution[17,19,55]. **b,** Critical thickness at which a system transitions from diffusion- to reaction-limited CO_2 transport (Da = 1) for different sorption and reaction processes: CO_2 reaction to form carbonate, CO_2 reaction with liquid amine, and limiting reaction rate of carbonic anhydrase enzyme[19,56–58]. Gas dissolution kinetics in water are rapid, and the equivalent critical thickness of water is below 1 nm. Typical thickness ranges for conventional liquid membranes (10–100 μm) and the thinnest membranes in this work (190 nm) are also shown.

The physical dissolution mechanism of gases in liquid water membranes allows them to avoid the reaction-rate limitations encountered in membranes that rely on reaction-facilitated transport of a carrier species. Transport limitations in these systems can be described by the Damköhler number (Da) which quantifies the ratio of reactive transport to diffusive transport and can be calculated by

$$\mathrm{Da} = \frac{k_r l^2}{D} \quad (7)$$

where k_r is the rate constant for the gas interacting with the liquid (s^{-1}), l is the liquid film thickness (m), and D is the diffusivity of a gas through the liquid ($m^2\ s^{-1}$). When the Damköhler number is much greater than unity, transport is diffusion limited. For a Damköhler number less than unity, the system is reaction rate limited, a regime that results in decreased selectivity for CO_2 over non-reactive species. In systems governed by amine- or carbonate-based chemistry, transport becomes limited by CO_2 reaction rates even at high thicknesses of 10–100 μm due to the relatively slow reaction rates (Figure 4b). The carbonic anhydrase enzyme enables more rapid carbonate reaction kinetics in liquid membranes, but the system will still become reaction-rate limited at low thicknesses. In contrast, transport in liquid water membranes relies on physical dissolution of CO_2 which has a rate constant on the order of $10^{10}\ s^{-1}$ so the system does not become dissolution rate limited at thicknesses above 1 Å[59]. Thus, water membranes are unique from other materials in that they can be fabricated as ultrathin layers, such as the 190-nm thick membranes demonstrated in this work, to increase permeance without encountering reaction rate limitations that limit permeance and reduce selectivity.

Scalability and mixed gas testing of liquid water membranes

Liquid water membranes can be implemented using any hydrophilic porous substrate with sufficiently small pores to maintain the water layer, making the approach inherently scalable. We demonstrated this principle using commercially available large-area membranes. Commercially produced hydrophilic polyvinylidene fluoride (PVDF) and polyethersulfone (PES) membranes were tested in gas separations after filling the pores with liquid water. PVDF and PES membranes were chosen because of the following: (1) they are commercially produced in large sheets (Figure 5a) by a scalable phase inversion process, (2) they are modified to be hydrophilic by the commercial supplier (Figure 5a, inset), and (3) they have sub-micron pore sizes (Figure 5b,c) which allow for stabilization of the liquid water layer.

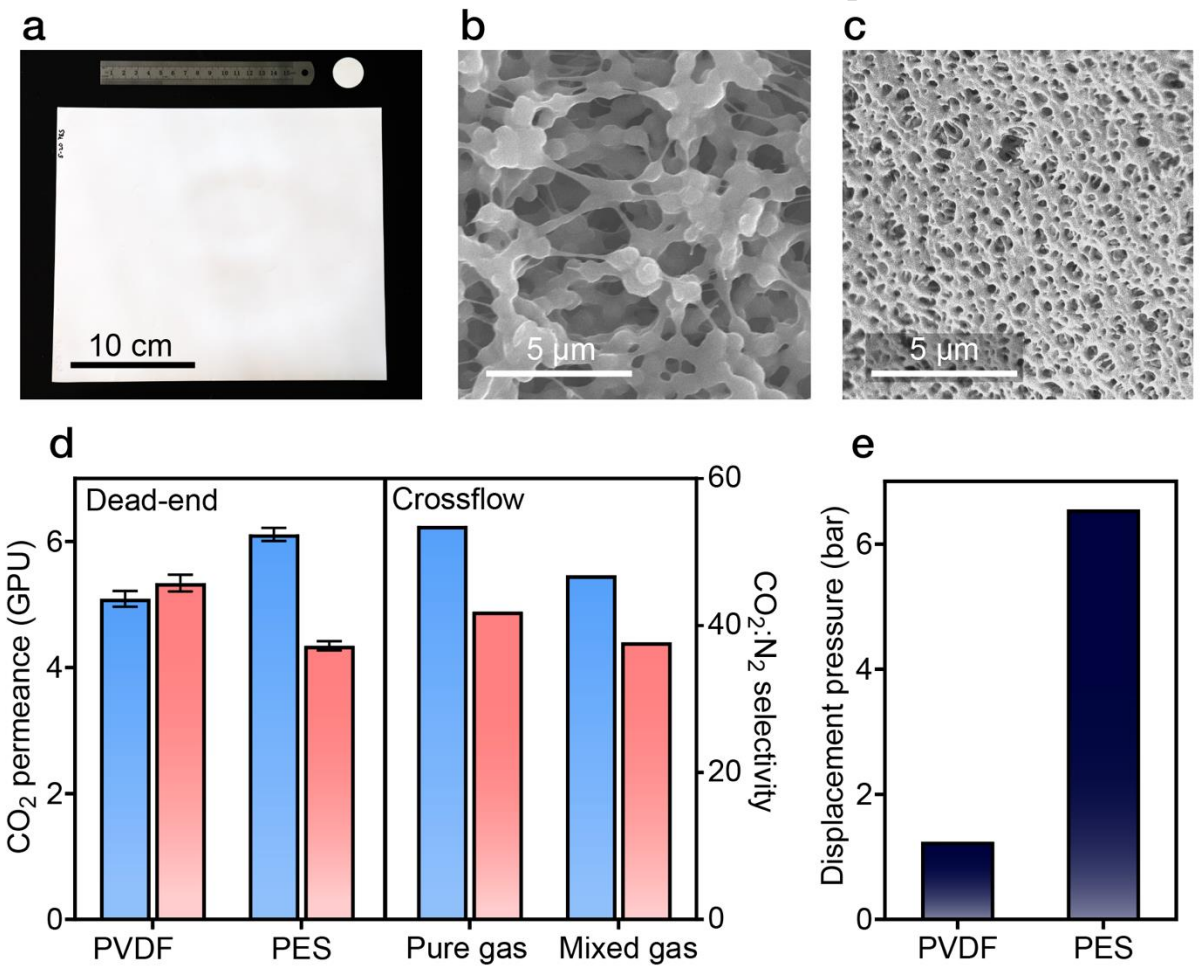

Fig. 5 | Water membranes are scalable using commercial membrane substrates under single- and mixed-gas operation. a, Photograph of the hydrophilic polyvinylidene fluoride (PVDF) and polyethersulfone (PES) membrane samples. **b**,**c**, Scanning electron micrograph of the top surface of the hydrophilic PVDF and PES membranes, respectively. **d,** Measured CO_2 permeance and

CO_2:N_2 selectivity of PVDF and PES membranes with trapped water layers. Permeance and selectivity are shown using single-component gas feeds in a dead-end cell (left panel) and using both single-component and multicomponent gas feeds in a crossflow system (right panel, results only shown for PES). Error bars denote the mean ±1 s.d. for measurements from at least three distinct membrane samples. **e,** Measured displacement pressures of water for PVDF and PES membranes.

Testing with commercially available hydrophilic membranes showed that liquid water membranes demonstrate constant CO_2:N_2 selectivities around 40 regardless of the substrate used (Figure 5d, left panel), in agreement with membrane transport theory and our results with ceramic membranes. For the unoptimized microns-thick commercial membranes used in this work, the CO_2 permeance was relatively low (5.1 GPU for PVDF and 6.1 GPU for PES). We attribute this low permeance to the large thickness of the water layer, which likely filled the entire thickness of the hydrophilic membrane and resulted in a long diffusion pathway for gases. The thickness of the water layer in the commercial membranes was approximately 100 μm (Supplementary Table 6), compared to 190 nm for the fabricated membranes.

To further assess performance in realistic conditions, multicomponent gas testing under crossflow was conducted on a commercial PES membrane using a feed gas mixture of 90% N_2 and 10% CO_2 at a total pressure of 3.1 bar (Figure 5d, right panel). The mixed-gas CO_2/N_2 selectivity was approximately 40, consistent with single-component measurements, indicating minimal interaction between the two gases in the aqueous phase.

Pressure stability measurements showed water displacement pressures of 1.5 bar for PVDF and 6.6 bar for PES. These pressures are sufficiently high for low-pressure gas separation membrane applications but lower than those observed with alumina membranes due to the larger, polydisperse pore sizes that are vulnerable to gas breakthrough at lower pressures. Based on the wetting pressure, the largest pores in the PVDF and PES membranes are approximately 960 nm and 218 nm, respectively, far larger than the 40 nm pores used in fabricated membranes (Supplementary Table 6). Overall, results with commercial membranes show that large-scale porous substrates can be used as liquid water membranes, but further optimization to decrease the water layer thickness and membrane pore size is necessary to enable improved permeance and pressure tolerance.

Discussion

This work introduces a new class of liquid water membranes that draw inspiration from the natural CO_2 uptake processes in plants. By fabricating membranes with hydrophilic sub-100-nm pores, we show that a stable water layer can be maintained at pressures exceeding 72 bar. Selectivity in the liquid water membrane is based primarily on solubility, where CO_2 is up to 40 times more permeable than other gases, such as N_2, due to its uniquely high solubility in water. Gas permeance can be increased by decreasing the water layer thickness without compromising selectivity, and membranes with 190-nm thick water layers show gas permeances exceeding 11,000 GPU while maintaining CO_2:N_2, CO_2:CH_4, and CO_2:H_2 selectivities of 40, 26, and 31, respectively. Membranes exhibit stable performance under dry, high-pressure conditions over eight days and maintain performance under high CO_2 partial pressures and with mixed gas feed streams in crossflow. Moreover, commercial large-scale membranes can be used with liquid water, although further optimization is required to improve permeance and pressure tolerance.

Liquid water membranes show promise for addressing separation challenges in applications such as point-source carbon capture, biogas processing, natural gas sweetening, and syngas upgrading. In these applications, the high CO_2 permeance, humidity tolerance, and pressure stability demonstrated in the liquid membranes introduced in this work may enable substantial improvements in cost, energy efficiency, and reliability. Unlike many conventional systems, water membranes are inherently compatible with humid or water-saturated gas streams, potentially removing the need for dehumidification processes that are required in many gas separation applications. Moreover, because water is non-toxic and environmentally benign, this approach offers a sustainable and potentially regenerable alternative to solvent-based or polymeric membranes.

Future efforts should prioritize scaling fabrication methods, evaluating long-term reliability, and assessing performance in full-scale process environments. We demonstrate operation at pressures up to 72 bar without breakthrough, but condensation or dissolution of contaminants in the water layer (e.g., SO_2, H_2S, and light hydrocarbons) could reduce surface tension and lower that threshold. Long-term stability of the water layer, particularly under dry or low-humidity conditions should also be examined. With continued development, liquid water membranes may enable the high-performance gas separations essential for a sustainable economy.

Methods

Liquid water membrane preparation. Membranes were prepared by pipetting 20 µL of deionized water onto a hydrophilic porous support and allowing the water to wick into the pores. Commercially available flat-sheet anodic alumina (InRedox, CO, USA), hydrophilic polyethersulfone (Sterlitech PES00347100), and polyvinylidene fluoride (Millipore HVLP02500) membranes were tested without modification. Membranes with a thin (less than 1 µm) hydrophilic layer were fabricated using anodic alumina substrates with varying pore diameters (20, 40, 80, and 120 nm) and a thickness of 50 µm (InRedox, CO, USA). The substrates were rinsed with acetone, ethanol, and isopropyl alcohol before being dried with nitrogen gas. The substrates were then hydroxylated using a UV ozone cleaner (Ossila, Sheffield, UK) for 5 mins and placed in a 10% H_2O_2 solution at 40 °C for 15 minutes before being exposed to 1H,1H,2H,2H-perfluorodecyltriethoxysilane at a temperature of 130 °C and a vacuum pressure of 50 mTorr for 8 hours to create a hydrophobic layer of fluorocarbons on the anodic alumina membrane. All silane modifications were performed in the vapor phase using a chemical vapor deposition chamber (Supplementary Figure 17). After hydrophobic modification, platinum was then deposited on the membranes using a magnetron sputter coater (Leica ACE600, Germany) with varying incident angles of 65° to 85° with a target distance of 50 mm, a current of 35 mA, and argon as the sputtering gas. The angle of sputtering determined the depth of the platinum layer using geometric calculations confirmed with experimental measurements and imaging. Platinum sputtered membranes were then exposed to 10 mM thioglycolic acid in isopropyl alcohol for 3 hours to selectively modify the platinum layer to become hydrophilic. The membranes were then rinsed with isopropyl alcohol, dried with nitrogen gas, and placed on a hot plate set at 40 °C for a minimum of 3 hours before performance testing.

Displacement pressure measurements. The pressure at which the water layer is displaced from the pores of the membrane was determined by the measurement of abrupt changes in gas flow, up to 7×10^5 GPU for dry anodic alumina membranes (Supplementary Figure 18), from the permeate side of the membrane under applied pressure. The high-pressure (up to 75 bar) membrane holder is shown in Supplementary Figure 19. Membrane samples with a 13 mm diameter were loaded in the test cell, and pressure was applied using compressed nitrogen gas and held for at least 5 minutes at each pressure increment. Pressure was increased in increments of 0.7 bar until membrane failure was observed via rapid gas transport through the pores.

Gas permeance testing. Gas transport across the membrane was measured using a membrane flow cell (In Redox, 304 stainless membrane holder) immersed in a DI water bath to maintain a temperature of 22 ± 2 °C (Supplementary Figure 14). Single gas permeation testing was performed using H_2, CO_2, CH_4, N_2, and O_2 gases (Airgas Part HY UHP300, CD FG20, ME CP80, NI UHP300, and OX USP200 cylinders,

respectively). Fabricated thin membranes were oriented in the membrane cell with the thin, hydrophilic layer facing the permeate side to prevent condensation and accumulation of water on the feed side. Depending on the gas permeation rate, gas flux was measured using an electronic gas flow meter (Aalborg Digital Mass Flowmeter Part 503924), a bubble gas flow meter (Manual Bubble Flowmeter Part 20433-U), or by tracking the displacement of a water column on the permeate side. Transmembrane pressure was controlled by adjusting the feed-side pressure from 1 to 72 bar, while the permeate side was maintained at atmospheric pressure. Relative humidity was measured on the feed side using a high-pressure humidity sensor (Roscid Technologies HDR200). Humidity was controlled by bubbling the feed gas through 15 ml of water at temperatures of 25–50 °C. Gas flux was quantified in units of cm^3 (STP)/(cm^2·s), and permeance is shown in gas permeation units (GPU), where 1 GPU = 10^{-6} cm^3 (STP)/(cm^2·s·cmHg). Multicomponent gas testing under crossflow conditions was conducted using CO_2 and N_2 mass flow controllers on the feed side, with helium used as a sweep gas on the permeate side (Maxwell Robotics, Mixed Gas Permeation Analyzer, Austin, Texas, USA). Humidity was introduced to both the feed and permeate streams using water vaporizers and was maintained above 90% relative humidity, as measured by hygrometers installed on both sides of the membrane. Gas permeability and selectivity were determined by gas chromatography analysis of the permeate stream.

Membrane characterization. Membrane hydrophobicity was characterized with an optical tensiometer (Biolin Scientific, AZ, USA) using the sessile drop method with one water droplet of 10 μL. The top surface of the membrane was imaged using field-emission scanning electron microscopy (SEM) from a JEOL JSM-7401F (Tokyo, Japan). The membrane cross section and thickness of the platinum layer was imaged using scanning transmission electron microscopy (STEM) (FEI Co. Talos F200X 200keV). X-ray photoelectron spectroscopy (XPS) (Kratos Supra, Kratos Analytical, UK) was performed by irradiating samples with a monochromatic Al K beam with a source energy of 1486.69 eV, and an X-ray beam power and resolution of 225 W.

Data availability statement

Source data are provided with this paper. Additional data supporting the findings of this study are available in the Supplementary Information and from the corresponding author upon request.

References

1. Galizia, M. *et al.* 50th Anniversary Perspective: Polymers and Mixed Matrix Membranes for Gas and Vapor Separation: A Review and Prospective Opportunities. *Macromolecules* **50**, 7809–7843 (2017).
2. Chen, G. *et al.* Solid-solvent processing of ultrathin, highly loaded mixed-matrix membrane for gas separation. *Science* **381**, 1350–1356 (2023).
3. Sandru, M. *et al.* An integrated materials approach to ultrapermeable and ultraselective CO2 polymer membranes. *Science* **376**, 90–94 (2022).
4. Ding, L. *et al.* MXene molecular sieving membranes for highly efficient gas separation. *Nat Commun* **9**, 155 (2018).
5. Zhu, B. *et al.* Boosting membrane carbon capture via multifaceted polyphenol-mediated soldering. *Nat Commun* **14**, 1697 (2023).
6. Sanders, D. F. *et al.* Energy-efficient polymeric gas separation membranes for a sustainable future: A review. *Polymer* **54**, 4729–4761 (2013).
7. Rochelle, G. T. Amine Scrubbing for CO2 Capture. *Science* **325**, 1652–1654 (2009).
8. Sholl, D. S. & Lively, R. P. Seven chemical separations to change the world. *Nature* **532**, 435–437 (2016).
9. Robeson, L. M. The upper bound revisited. *Journal of Membrane Science* **320**, 390–400 (2008).
10. Park, H. B., Kamcev, J., Robeson, L. M., Elimelech, M. & Freeman, B. D. Maximizing the right stuff: The trade-off between membrane permeability and selectivity. *Science* **356**, eaab0530 (2017).
11. Chamoun-Farah, A. *et al.* Amine functionalized supported ionic liquid membranes (SILMs) for CO2/N2 separation. *Journal of Membrane Science* **702**, 122758 (2024).
12. Ying, W. *et al.* Ionic Liquid Selectively Facilitates CO2 Transport through Graphene Oxide Membrane. *ACS Nano* **12**, 5385–5393 (2018).
13. Chen, X. *et al.* Polyolefin reweaved ultra-micropore membrane for CO2 capture. *Nat Commun* **16**, 282 (2025).

14. Bachman, J. E., Smith, Z. P., Li, T., Xu, T. & Long, J. R. Enhanced ethylene separation and plasticization resistance in polymer membranes incorporating metal–organic framework nanocrystals. *Nature Mater* **15**, 845–849 (2016).
15. Fortunato, R., Afonso, C. A. M., Reis, M. A. M. & Crespo, J. G. Supported liquid membranes using ionic liquids: study of stability and transport mechanisms. *Journal of Membrane Science* **242**, 197–209 (2004).
16. Neves, L. A., Crespo, J. G. & Coelhoso, I. M. Gas permeation studies in supported ionic liquid membranes. *Journal of Membrane Science* **357**, 160–170 (2010).
17. Chamoun-Farah, A., Cañada, L. M., Brennecke, J. F. & Freeman, B. D. Supported ionic liquid membranes (SILMs) with exceptional selectivity and permeability for dilute CO2 separations. *Journal of Membrane Science* **727**, 124081 (2025).
18. Ward, W. J. & Robb, W. L. Carbon Dioxide-Oxygen Separation: Facilitated Transport of Carbon Dioxide across a Liquid Film. *Science* **156**, 1481–1484 (1967).
19. Hanioka, S. *et al.* CO2 separation facilitated by task-specific ionic liquids using a supported liquid membrane. *Journal of Membrane Science* **314**, 1–4 (2008).
20. Rosenthal, J. J. *et al.* Improving blowout pressure in supported ionic liquid membranes for light paraffin fractionation. *Journal of Membrane Science* **717**, 123624 (2025).
21. Pan, Y. *et al.* A Large and Persistent Carbon Sink in the World's Forests. *Science* **333**, 988–993 (2011).
22. Hetherington, A. M. & Woodward, F. I. The role of stomata in sensing and driving environmental change. *Nature* **424**, 901–908 (2003).
23. Nobel, P. S. *Physicochemical & Environmental Plant Physiology*. (Academic Press, 1999).
24. Evans, J. R. Mesophyll conductance: walls, membranes and spatial complexity. *New Phytologist* **229**, 1864–1876 (2021).

25. Vesala, T. *et al.* Effect of Leaf Water Potential on Internal Humidity and CO2 Dissolution: Reverse Transpiration and Improved Water Use Efficiency under Negative Pressure. *Front. Plant Sci.* **8**, (2017).
26. Wheeler, T. D. & Stroock, A. D. The transpiration of water at negative pressures in a synthetic tree. *Nature* **455**, 208–212 (2008).
27. Wang, Y., Lee, J., Werber, J. R. & Elimelech, M. Capillary-driven desalination in a synthetic mangrove. *Science Advances* **6**, eaax5253 (2020).
28. Fu, Y. *et al.* Ultra-thin enzymatic liquid membrane for CO2 separation and capture. *Nat Commun* **9**, 990 (2018).
29. Chamoun-Farah, A., Cañada, L. M., Brennecke, J. F. & Freeman, B. D. Supported ionic liquid membranes (SILMs) with exceptional selectivity and permeability for dilute CO2 separations. *Journal of Membrane Science* **727**, 124081 (2025).
30. Qian, J., Wang, R., Wu, H., Wang, F. & Elimelech, M. Molecular simulations reveal gas transport mechanisms in polyamide membranes. *Journal of Membrane Science* **731**, 124056 (2025).
31. Bernardo, P., Drioli, E. & Golemme, G. Membrane Gas Separation: A Review/State of the Art. *Ind. Eng. Chem. Res.* **48**, 4638–4663 (2009).
32. Kadirkhan, F. *et al.* CO2 Plasticization Resistance Membrane for Natural Gas Sweetening Process: Defining Optimum Operating Conditions for Stable Operation. *Polymers* **14**, 4537 (2022).
33. Park, S. *et al.* Mesoporous silica modified alumina improves pressure stability of supported ionic liquid membranes. *Journal of Membrane Science* **710**, 123138 (2024).
34. Tariq, M. *et al.* Surface tension of ionic liquids and ionic liquid solutions. *Chemical Society Reviews* **41**, 829–868 (2012).
35. Faramarzi, H. *et al.* An Overview of Practical Aspects of the Design and Application of Polymeric/Ceramic Supports in Supported Liquid Membranes for Gas Separation. *Ind. Eng. Chem. Res.* **62**, 12443–12461 (2023).

36. Maserati, L., Meckler, S. M., Bachman, J. E., Long, J. R. & Helms, B. A. Diamine-Appended Mg2(dobpdc) Nanorods as Phase-Change Fillers in Mixed-Matrix Membranes for Efficient CO2/N2 Separations. *Nano Lett.* **17**, 6828–6832 (2017).
37. Soleimani, R. & Saeedi Dehaghani, A. H. A theoretical probe into the separation of CO2/CH4/N2 mixtures with polysulfone/polydimethylsiloxane–nano zinc oxide MMM. *Sci Rep* **13**, 9543 (2023).
38. He, G. *et al.* High-permeance polymer-functionalized single-layer graphene membranes that surpass the postcombustion carbon capture target. *Energy & Environmental Science* **12**, 3305–3312 (2019).
39. White, L. S., Amo, K. D., Wu, T. & Merkel, T. C. Extended field trials of Polaris sweep modules for carbon capture. *Journal of Membrane Science* **542**, 217–225 (2017).
40. Ghalei, B. *et al.* Enhanced selectivity in mixed matrix membranes for CO2 capture through efficient dispersion of amine-functionalized MOF nanoparticles. *Nat Energy* **2**, 1–9 (2017).
41. Bushell, A. F. *et al.* Gas permeation parameters of mixed matrix membranes based on the polymer of intrinsic microporosity PIM-1 and the zeolitic imidazolate framework ZIF-8. *Journal of Membrane Science* **427**, 48–62 (2013).
42. Rahimalimamaghani, A., Ramezani, R., Tanaka, D. A. P. & Gallucci, F. Carbon Molecular Sieve Membranes for Selective CO2/CH4 and CO2/N2 Separation: Experimental Study, Optimal Process Design, and Economic Analysis. *Ind. Eng. Chem. Res.* **62**, 19116–19132 (2023).
43. Wang, Z., Ren, H., Zhang, S., Zhang, F. & Jin, J. Polymers of intrinsic microporosity/metal–organic framework hybrid membranes with improved interfacial interaction for high-performance CO2 separation. *J. Mater. Chem. A* **5**, 10968–10977 (2017).
44. Lu, J. *et al.* Preparation of Amino-Functional UiO-66/PIMs Mixed Matrix Membranes with [bmim][Tf2N] as Regulator for Enhanced Gas Separation. *Membranes* **11**, 35 (2021).
45. Lin, H., Van Wagner, E., Freeman, B. D., Toy, L. G. & Gupta, R. P. Plasticization-Enhanced Hydrogen Purification Using Polymeric Membranes. *Science* **311**, 639–642 (2006).

46. Reijerkerk, S. R., Knoef, M. H., Nijmeijer, K. & Wessling, M. Poly(ethylene glycol) and poly(dimethyl siloxane): Combining their advantages into efficient CO2 gas separation membranes. *Journal of Membrane Science* **352**, 126–135 (2010).

47. Lau, C. H. *et al.* Silica Nanohybrid Membranes with High CO2 Affinity for Green Hydrogen Purification. *Advanced Energy Materials* **1**, 634–642 (2011).

48. Kniep, J. *et al. FIELD TESTS OF MTR MEMBRANES FOR SYNGAS SEPARATIONS: Final Report of CO2-Selective Membrane Field Test Activities at the National Carbon Capture Center*. (2017).

49. Lin, H. *et al.* Transport and structural characteristics of crosslinked poly(ethylene oxide) rubbers. *Journal of Membrane Science* **276**, 145–161 (2006).

50. Kaser, S. J. *et al.* High-Selectivity CO2 Mixture Separations by a Guanylated Polymer of Intrinsic Microporosity (PIM-G) Membrane. *Macromolecules* **57**, 10023–10031 (2024).

51. Koros, W. J. & Zhang, C. Materials for next-generation molecularly selective synthetic membranes. *Nature Mater* **16**, 289–297 (2017).

52. Song, S. *et al.* High-performance H2/CO2 separation from 4-nm-thick oriented Zn2(benzimidazole)4 films. *Science Advances* **10**, eads6315 (2024).

53. Han, Y., Salim, W., Chen, K. K., Wu, D. & Ho, W. S. W. Field trial of spiral-wound facilitated transport membrane module for CO2 capture from flue gas. *Journal of Membrane Science* **575**, 242–251 (2019).

54. Khalilpour, R. *et al.* Membrane-based carbon capture from flue gas: a review. *Journal of Cleaner Production* **103**, 286–300 (2015).

55. Kasahara, S., Kamio, E., Ishigami, T. & Matsuyama, H. Amino acid ionic liquid-based facilitated transport membranes for CO2 separation. *Chem. Commun.* **48**, 6903–6905 (2012).

56. Abu-Arabi, M. K., Al-Jarrah, A. M., El-Eideh, M. & Tamimi, A. Physical Solubility and Diffusivity of CO_2 in Aqueous Diethanolamine Solutions. *J. Chem. Eng. Data* **46**, 516–521 (2001).

57. Yuksel Orhan, O. & Alper, E. Kinetics of reaction *between CO2* and ionic liquid-carbon dioxide binding organic liquid hybrid systems: Analysis of gas-liquid absorption and stopped flow experiments. *Chemical Engineering Science* **170**, 36–47 (2017).

58. Silverman, D. N. & Lindskog, S. The catalytic mechanism of carbonic anhydrase: implications of a rate-limiting protolysis of water. *Acc. Chem. Res.* **21**, 30–36 (1988).

59. Mitchell, M. J., Jensen, O. E., Cliffe, K. A. & Maroto-Valer, M. M. A model of carbon dioxide dissolution and mineral carbonation kinetics. *Proceedings of the Royal Society A: Mathematical, Physical and Engineering Sciences* **466**, 1265–1290 (2009).

Acknowledgements

K.P.L. appreciates support from the National Aeronautics and Space Administration (NASA) via the NASA Space Technology Graduate Research Opportunity (NSTGRO) fellowship. A.P.S. gratefully acknowledges support from the U.S. National Science Foundation under CAREER Award No. CBET-2442780. We thank Dragan Mejic at the University of Colorado Boulder Chemical Engineering Instrument Shop for his assistance in manufacturing components of the high-pressure gas permeation cell. We also thank Praveen Kumar at Colorado School of Mines for assistance with transmission electron microscopy. This work was authored in part by the National Laboratory of the Rockies (NLR), operated by Alliance for Sustainable Energy, LLC, for the U.S. Department of Energy (DOE) under Contract No. DE-AC36-08GO28308. This work was supported by the Transformational Laboratory Directed Research and Development (TLDRD) Program at NLR. The views expressed in the article do not necessarily represent the views of the DOE or the U.S. Government. The U.S. Government retains and the publisher, by accepting the article for publication, acknowledges that the U.S. Government retains a nonexclusive, paid-up, irrevocable, worldwide license to publish or reproduce the published form of this work, or allow others to do so, for U.S. Government purposes.

Author contributions

K.P.L. designed and conducted membrane fabrication, characterization, and permeation experiments, and analyzed the results. A.P.S. conceived the project and provided scientific

supervision throughout the study. M.A., Y.T., and P.O.S. performed permeation experiments and contributed to analysis and interpretation of the transport data with supervision from M.P., A.R., and A.P.S. M.S.M. fabricated membranes, conducted fabrication-related characterization and analyses, and contributed to manuscript writing. J.N.S. performed XPS measurements and analysis. S.R.N. conducted SEM imaging and analysis. K.P.L., M.S.M., M.A., Y.T., J.N.S., S.R.N., P.O.S., M.P., A.R., and A.P.S. discussed the results. K.P.L., M.S.M., and A.P.S. wrote the manuscript; all authors revised and approved the final version.

Competing interests

M.S.M., M.A., J.N.S., S.R.N., Y.T., P.O.S., M.P., and A.R. declare no competing financial interests. K.P.L and A.P.S are cofounders, board members, and officers for Osmopure Technologies Inc., and they have equity holdings related to the materials in this work.

Figure captions

Fig. 1. | Water membranes for gas separations. a, Schematic diagram of CO_2 uptake in trees where CO_2 dissolves into water-filled nanochannels in the wall of leaf mesophyll cells. Capillary forces and water evaporation generate lower pressures inside the cell water channels, P_{cell}, than in the atmosphere, P_{atm}. These negative pressures, up to 150 bar, drive water uptake through the roots and water flow up the xylem water channels. **b**, Schematic diagram of water-based membranes for gas separations, where a layer of water is stabilized within hydrophilic pores. To transport through the membrane, feed gases must dissolve in the water, diffuse through the layer in the aqueous phase, and desorb on the permeate side of the membrane. CO_2 is preferentially transported because of its higher solubility in water compared to other gases.

Fig. 2 | Gas separation performance and robustness of the water membrane. a, Schematic of testing setup for gas transport measurements. Inset shows membranes where water fills the entire pore thickness (top) and membranes selectively coated with a hydrophilic water-trapping layer in the upper pore (bottom). In both cases, the pore radius, r, and water layer thickness, l, could be controlled. **b**, Scanning electron micrograph of the top surface of the anodic alumina membrane with a 40-nm pore diameter. **c,** Scanning transmission electron microscopy high-angle annular dark-field image showing a cross section of the upper pore. **d**, Contact angle of water on the hydrophilic top surface of the membrane (top) and on the hydrophobic bottom surface of the membrane (bottom). **e**, Measured displacement pressure of the water layer as a function of pore diameter for fabricated membranes (symbols). Theoretical displacement pressures obtained from the Young–Laplace equation using the surface tension of water (72 mN/m) and ionic liquids (25 and 45 mN/m) are also shown[34]. **f**, Measured gas flux as a function of the feed gas pressure for fabricated membranes with 40-nm pore diameters and estimated water layer thicknesses of 287 nm. Lines show gas flux predicted using the solution-diffusion model. Gas flux was normalized to the membrane porosity of 12% so that reported values are representative of the water-filled active pore area. **g**, Measured gas permeance as a function of aqueous solubility for different gases using a membrane pore diameter of 40 nm and an estimated water layer thickness of 190 nm (symbols), and simulated permeance using the solution-diffusion model with a diffusion coefficient of 2.00×10^{-5} $cm^2 \cdot s^{-1}$ (line). **h**, Permeance as a function of the water layer thickness for measurements

(symbols) and simulations (lines). **i**, Long-term stability of liquid water membranes over 8 days of operation. Gas permeance was normalized to the initial value. Relative humidity in the feed was limited to less than 1% by continuously venting feed gas. Error bars denote the mean ±1 s.d. for measurements from at least three distinct membrane samples.

Fig. 3 | Water membranes exceed current permeance and selectivity limits. a, Permeance-selectivity trade-off for CO_2:N_2 with the water membranes studied in this work (blue stars) compared to common values found in the literature (black squares) and the following high performance membranes: Polaris[39], UiO-66-NH_2-M[40], ZIF-8[41], HZIF-8[5], CMS[42], and M-PEI[38]. The Robeson upper bound[9] assuming a thickness of 1 μm is also shown. **b**, Permeance-selectivity trade-off for CO_2:CH_4 compared to literature values and high performance membranes: HZIF-8[5], PIM-1/NH_2-UiO-66[43], ZIF-8[41], UiO-66-NH_2@IL/PIM-1[44], and M-PEI[38]. **c**, Permeance-selectivity performance for CO_2:H_2 compared to the permeance-selectivity upper bound[45] and high performance membranes: PEO/PDMS[46], PEGMA/Particles[47], Polaris[48], and PEGDA/PEGMA[49]. Gas flux is normalized to the active pore area of the membrane based on a porosity of 12%.

Fig. 4 | Sorption capacity and dissolution kinetics of CO_2 in water. a, CO_2 permeability (Barrer) as a function of CO_2 partial pressure in supported ionic liquid and water membranes. At high CO_2 partial pressure, ionic liquids with high CO_2 solubility can become saturated resulting in lower CO_2 permeability. Water maintains constant CO_2 permeability at high pressure because CO_2 transport is driven by physical dissolution[17,19,55]. **b,** Critical thickness at which a system transitions from diffusion- to reaction-limited CO_2 transport (Da = 1) for different sorption and reaction processes: CO_2 reaction to form carbonate, CO_2 reaction with liquid amine, and limiting reaction rate of carbonic anhydrase enzyme[19,56–58]. Gas dissolution kinetics in water are rapid, and the equivalent critical thickness of water is below 1 nm. Typical thickness ranges for conventional liquid membranes (10–100 μm) and the thinnest membranes in this work (190 nm) are also shown.

Fig. 5 | Water membranes are scalable using commercial membrane substrates under single- and mixed-gas operation. a, Photograph of the hydrophilic polyvinylidene fluoride (PVDF) and

polyethersulfone (PES) membrane samples. **b**,**c**, Scanning electron micrograph of the top surface of the hydrophilic PVDF and PES membranes, respectively. **d,** Measured CO_2 permeance and CO_2:N_2 selectivity of PVDF and PES membranes with trapped water layers. Permeance and selectivity are shown using single-component gas feeds in a dead-end cell (left panel) and using both single-component and multicomponent gas feeds in a crossflow system (right panel, results only shown for PES). Error bars denote the mean ±1 s.d. for measurements from at least three distinct membrane samples. **e,** Measured displacement pressures of water for PVDF and PES membranes.

Editorial Summary

Ultrathin layers of liquid water confined in nanoporous membranes enable fast, selective, and stable separation of carbon dioxide from other gases.

Peer Review Information: *Nature Communications* thanks Zhengmao Lu and the other, anonymous, reviewer(s) for their contribution to the peer review of this work. A peer review file is available.